https://doi.org/10.5194/egusphere-2026-2286
Preprint. Discussion started: 28 May 2026

# PecubeGUI: a user interface for the Pecube thermal-kinematic model and advanced low-temperature thermochronometer predictions

Maxime Bernard[1, 5], Pieter van der Beek[1], Cody Colleps[1,6], Xavier Robert[2], Kerry Gallagher[3] William Guenthner[4], Julien Amalberti[1], Georgina E. King[5]

[1]Institut für Geowissenschaften, Universität Potsdam, Karl-Liebknecht-Straße 24–25, D-14476 Potsdam, Golm, Germany.

[2]Institut des Sciences de la Terre (ISTerre), Univ. Grenoble Alpes, Univ. Savoie Mont Blanc, CNRS, IRD, Univ. Gustave Eiffel, Grenoble, France.
[3]Géosciences Rennes/OSUR, Université de Rennes, France.
[4]Department of Earth Science & Environmental Change, University of Illinois at Urbana-Champaign, Champaign, Illinois, USA.
[5]Institute of Earth Surface Dynamics, Université de Lausanne, Switzerland.

[6]Department of Geoscience, University of Nevada, Las Vegas, NV 89154-4010, USA.

*Correspondence to*: Maxime Bernard (maxime.bernard@unil.ch)

## Abstract.

Thermochronology offers critical constraints on rock cooling and exhumation histories, enabling quantitative assessments of landscape evolution and its interactions with tectonic and climatic forcings. These interpretations increasingly rely on numerical models capable of linking measured thermochronometric data to realistic thermal and kinematic scenarios. Among such tools, the Pecube code provides a unique 3D thermal-kinematic framework that explicitly couples tectonic and geomorphic processes with predicted thermochronometric observables, which has been widely used for reconstructing the tectonic and topographic evolution of mountain belts as well as crustal thermal structure. In this contribution, we introduce PecubeGUI, a new open-access graphical user interface (GUI) that modernises and greatly enhances the accessibility of Pecube. Alongside the interface, we present substantial updates to Pecube, including the implementation of contemporary radiation-damage models for apatite and zircon (U–Th)/He thermochronometers, multi-kinetic models for fission-track annealing, and the integration of ultra-low temperature thermochronometers such as the apatite $^4$He/$^3$He and trapped-charge methods, the latter being in active development. These additions expand the ability of Pecube to resolve low-temperature cooling signals, particularly at Quaternary timescales, where increased temporal resolution is essential for understanding landscape evolution.

By lowering the technical barrier to Pecube modelling and broadening the toolkit available to users, PecubeGUI aims to foster wider adoption and stimulate new applications across the thermochronology, geomorphology, and tectonics communities.

https://doi.org/10.5194/egusphere-2026-2286
Preprint. Discussion started: 28 May 2026

## 1 Introduction

Quantifying rates of landscape evolution and their interactions with tectonic and climatic processes is essential for understanding the primary controls on Earth surface dynamics. Low-temperature thermochronology provides a powerful set of techniques for constraining rock exhumation from depth to the surface, reflecting the combined effect of rock uplift driven by tectonic processes and erosion driven by surface processes (e.g., Ault et al, 2018). To a first order, thermochronology measures the concentration of daughter products, produced by radioactive decay, relative to that of their parent isotopes in a mineral, yielding an age that corresponds to the time at which the sample passed through the closure temperature (Tc) of the employed system (e.g., Dodson, 1973; Reiners and Brandon, 2006). But this simple interpretation becomes more complex in settings where rocks cool slowly through the partial retention zone (PRZ) of the daughter products, and observed ages reflect a balance between their diffusive loss (controlled primarily by temperature) and their accumulation by radioactive decay (e.g., Fitzgerald and Malusà, 2019; Reiners and Brandon, 2006).

Additional complexity arises from the fact that daughter-product retention is influenced by factors beyond temperature alone. For example, the zircon and apatite (U-Th)/He systems are strongly affected by radiation damage created in the crystal lattice during U and Th decay. These defects can act as traps that increase helium retentivity and closure temperature, but also as preferred pathways that enhance helium diffusion (e.g., Flower et al., 2023a, b; Gautheron et al., 2020; Guenthner et al., 2013; Shuster et al., 2006). Over the past decades, substantial progress has been made in quantifying the effect of radiation damage accumulation and annealing through the development of numerical models capable of capturing these effects (Flowers et al., 2009; Gautheron et al., 2009; Ginster et al., 2019; Guenthner et al., 2013; Shuster et al., 2006; Willett et al., 2017).

Interpretation of thermochronometer data commonly relies on numerical models that reconstruct thermal histories capable of reproducing the observed data. Over the last two decades, three software packages have become standard tools within the thermochronology community. The thermal modelling codes HeFTy (Ketcham, 2005) and QTQt (Gallagher, 2012) implement frequentist and Bayesian approaches, respectively, in which large ensembles of cooling histories are randomly generated and evaluated using appropriate diffusion and annealing models. Comprehensive reviews of their methodologies and applications are provided elsewhere (Abbey et al., 2023; Gallagher, 2012; Ketcham, 2024; Murray et al., 2022; Vermeesch and Tian, 2014). Although both tools are highly effective for modelling thermochronometer data, they predict cooling histories only which cannot be directly translated into exhumation histories and are restricted to modelling of single samples or vertical profile datasets (although efforts have been made to model spatially distributed data, Ketcham; 2024; Stephenson et al., 2006). Consequently, while these approaches provide predictions of the main control on the data, i.e., the thermal history, they do not explicitly address the geomorphic or tectonic processes responsible for the reconstructed thermal evolution. The latter requires a user to define or infer more model specific parameters than just time-temperature points.

Pecube is a 3D thermal-kinematic modelling code specifically designed to simulate rock cooling histories and thermochronometer data resulting from prescribed tectonic and geomorphic scenarios (Braun, 2003; Braun et al., 2012). Since its initial development by Braun (2003), Pecube has offered the key advantage of predicting thermochronometer data arising from thermal perturbations generated by a prescribed rock-uplift filed combined with an evolving surface topography. In its early versions, rock advection was restricted to the vertical axis, and thermochronometer predictions were limited to mica Ar-Ar, apatite fission-track, and apatite (U-Th)/He ages. The last major update of Pecube (version 4; Braun et al., 2012) expanded the applicability of Pecube to (1) spatially variable rock-uplift fields including flexural isostasy (Braun and Robert, 2005), (2) fault-bounded domains, and (3) additional thermochronometric systems such as zircon (U-Th)/He (Reiners et al., 2004), and Ar-Ar on hornblende and K-feldspar (Harrison, 1982; Lovera et al., 1991). A comprehensive overview of these updates is provided in Braun et al. (2012). While Pecube forward models can be performed to test main hypotheses, the complexity of a dataset and the range of plausible geomorphic and tectonic scenarios that agree with the data often require an inversion approach, in which thousands of models are generated and evaluated using an objective function. Pecube is coupled with the neighbourhood algorithm (Sambridge, 1999a) to guide the exploration of a parameter space and optimise the inversion procedure.

Pecube has been extensively used to investigate the structural evolution of mountain belts (e.g., Campani et al., 2010; Herman et al., 2010a; Robert et al., 2011; Wolff et al., 2021), the development and modification of topographic relief (e.g., McDannell et al., 2018; Schildgen et al., 2010; Valla et al., 2011), and the influence of crustal thermal properties and fluid flow on rock exhumation rate inferred from thermochronometer data (e.g., Braun et al., 2016; Łuszczak et al., 2017; Whipp and Ehlers, 2007). Despite its widespread use, Pecube still lacks a user-friendly interface comparable to HeFTy or QTQt, limiting accessibility for the thermochronology community. Furthermore, since the last release, substantial progress has been made in the development of diffusion and annealing models. Notably, advanced models incorporating radiation-damage effects have been developed for the apatite (Flowers et al., 2009; Gautheron et al., 2009; Shuster et al., 2006; Willett et al., 2017) and zircon (U-Th)/He systems (Ginster et al., 2019; Guenthner et al., 2013), and updated annealing models for apatite fission tracks (Ketcham et al., 2007) have become available. In addition, new ultra-low-temperature (20-100°C) thermochronometric methods, including $^{4}$He/$^{3}$He (Shuster et al., 2004) and trapped-charge thermochronometry (e.g., King et al., 2016), now enable detailed reconstruction of Quaternary-scale landscape evolution, including constraints on valley incision (e.g., Schildgen et al., 2010; Shuster et al., 2011), glacial modification of topography (e.g., Herman et al., 2010b; Valla et al., 2011, 2012; Wen et al., 2024), or recent shallow exhumation in foreland foreland fold-and-thrust belts (Bouscary et al., 2024). However, the kinetic models currently available in Pecube v4 are outdated, limiting its applicability for slowly exhuming settings, samples with high U-Th contents, and short (i.e., Quaternary) timescales.

In this contribution, we present a newly developed graphical user interface for Pecube, called PecubeGUI, along with significant updates to the thermal and thermochronometer-prediction modules of Pecube, including implementation of multi-kinetic annealing/diffusion models and integration of recently developed thermochronometers. PecubeGUI is open-source and freely available, allowing users to inspect the code implementation and contribute to ongoing development.

## 2 Framework

### 2.1 Overview of the PecubeGUI package

The PecubeGUI package consists of three interacting components: the Python-based user interface, the Pecube thermal-kinematic model, and an external program for thermochronometer data predictions (CalcAge; Fig. 1); the latter two are written in Fortran90. The GUI operates as an external layer that communicates with the original Pecube directory structure (Braun et al., 2012) and provides all required input parameters through the standard Pecube input file format. Pecube computes thermal histories for particles ending up at each surface node or at user-specified locations at the end of the simulation.

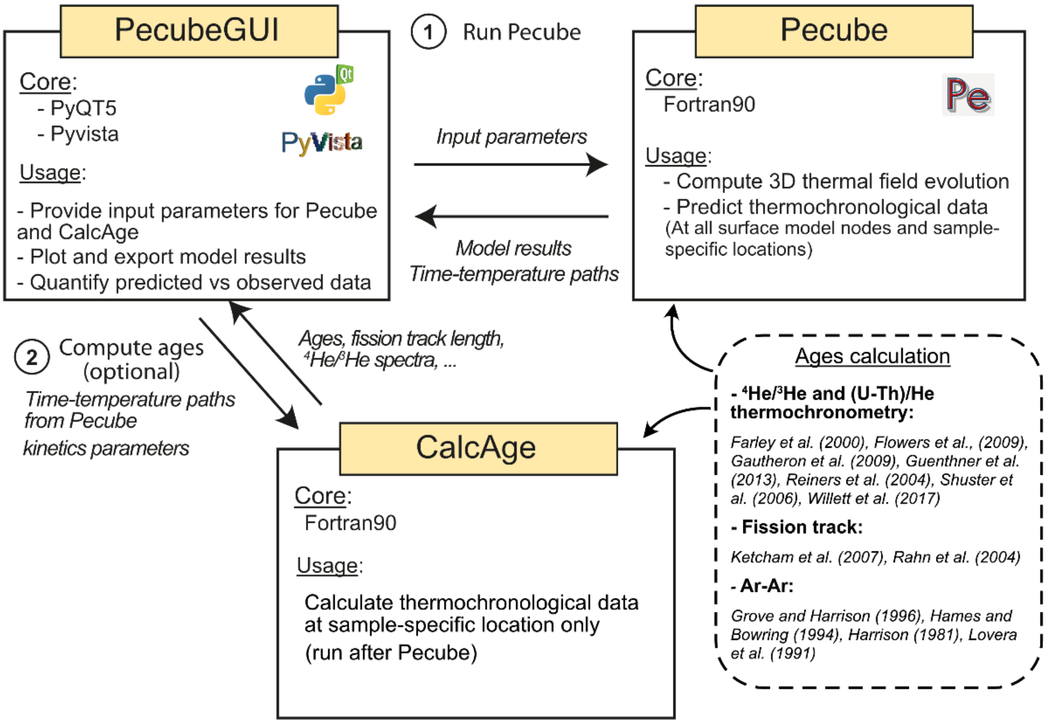

**Figure 1.** Structure and framework of the PecubeGUI package. The package is divided into three programs: two Fortran90 codes, Pecube and CalcAge, and the graphical user interface written in Python. The thermal-kinematic model Pecube solves the 3D heat-transport equation given an input geomorphic-tectonic evolution scenario, and predicts thermochronometry data at each surface model node or at sample locations. CalcAge computes thermochronometery data only at sample locations using time-temperature paths output from Pecube and can be run independently after a Pecube run. Pecube and CalcAge share the subroutines that calculate thermochronometry data. The graphical user interface (PecubeGUI) is designed to communicate between the user, Pecube and CalcAge.

A main advancement of this work is the implementation of an updated production-diffusion (PD) model for helium that incorporates radiation-damage accumulation and annealing (see Sect. 2.4). In the PecubeGUI package, rock thermal histories and thermochronometer data are predicted by Pecube at all surface nodes or at sample locations as originally designed by Braun (2003). The CalcAge program has been added to allow recalculation of thermochronometer data at sample locations and can be called after a Pecube run. This setup allows users to modify kinetic parameters and recalculate ages without rerunning the full thermal-kinematic model, thus optimising computation time. CalcAge is executed via the GUI and reads time-temperature paths from the output file generated by Pecube at the end of each simulation (i.e., “TimeTemperaturePaths.csv”). CalcAge can be called only when predicting data at sample locations and not when predictions are made at all surface nodes. To ensure consistency and facilitate future updates of the PD model or other kinetic formulations, CalcAge and Pecube share the same underlying subroutines to calculate thermochronometer data (Fig. 1).

In the next sections, we describe each component of the framework in more detail.

## 2.2 Pecube

The Pecube core solves the heat-transport equation in 3D to predict time-temperature paths for a user-imposed geomorphic-tectonic scenario (Braun, 2003). The heat-transport equation includes thermal advection in three dimensions ($x$, $y$, $z$), such that:

$$\frac{\partial T}{\partial t} + u\frac{\partial T}{\partial x} + v\frac{\partial T}{\partial y} + w\frac{\partial T}{\partial z} = \frac{\partial}{\partial x}\kappa\frac{\partial T}{\partial x} + \frac{\partial}{\partial y}\kappa\frac{\partial T}{\partial y} + \frac{\partial}{\partial z}\kappa\frac{\partial T}{\partial z} + H_p, \tag{1}$$

where $T$ is temperature, $t$ is time, $u$, $v$, and $w$ are the components of the velocity field representing the relative motion of rock in the x, y and z directions respectively, with respect to a fixed base, $\kappa$ is thermal diffusivity, and $H_p$ is heat production (Braun et al., 2012). Thermal diffusivity is derived from rock thermal conductivity ($k$), density ($\rho$) and heat capacity (c); $\kappa = k / \rho c$, and has dimensions of $L^2 t^{-1}$. The relevant form of the heat production term in equation (1) has dimension of $T t^{-1}$ (see Sect. 3.1.2).

PecubeGUI was developed from Pecube version 4.2, which corresponds to the most recent major release of Pecube. The kinetic models for predicting thermochronometry data currently available in Pecube v4.2 are outdated, limiting the application of Pecube. To address these limitations, we updated the Pecube code (v4.3) in parallel with the development of PecubeGUI. The new version incorporates radiation-damage models for apatite and zircon (U-Th)/He thermochronometry (Flowers et al., 2009; Gautheron et al., 2009; Guenthner et al., 2013; Shuster et al., 2006; Willett et al., 2017), the most recent annealing model for fission tracks in apatite (Ketcham et al., 2007), and a model predicting $^4$He/$^3$He degassing spectra in apatite. All these models are now available for both forward and inverse modelling within Pecube. Active development of Pecube focuses on implementation of trapped-charge dating methods, which are currently not available.

## 2.3 PecubeGUI: the graphical user interface (GUI)

PecubeGUI is implemented as a PyQt5 application. In addition to the wide range of open-source python libraries, the Qt application framework offers substantial flexibility and a versatile environment for constructing a user-friendly interface. For example, the Pyvista library (Sullivan and Kaszynski, 2025) is used to read and interactively visualise 3D models from vtk files generated by Pecube, enabling straightforward integration of 3D visualisation within the PyQT5 application.

The GUI is designed both to provide input parameters to Pecube and to read and process Pecube output. In addition, it offers a suite of tools that assists users in setting up, inspecting, and validating their model configurations prior to execution. For instance, users can import topography from raster files and visualise prescribed topographic-evolution scenarios (see Sect. 3.1.1). For accessibility and maintainability, the PecubeGUI code is organised into libraries addressing specific functionalities of the interface (Fig. 2).

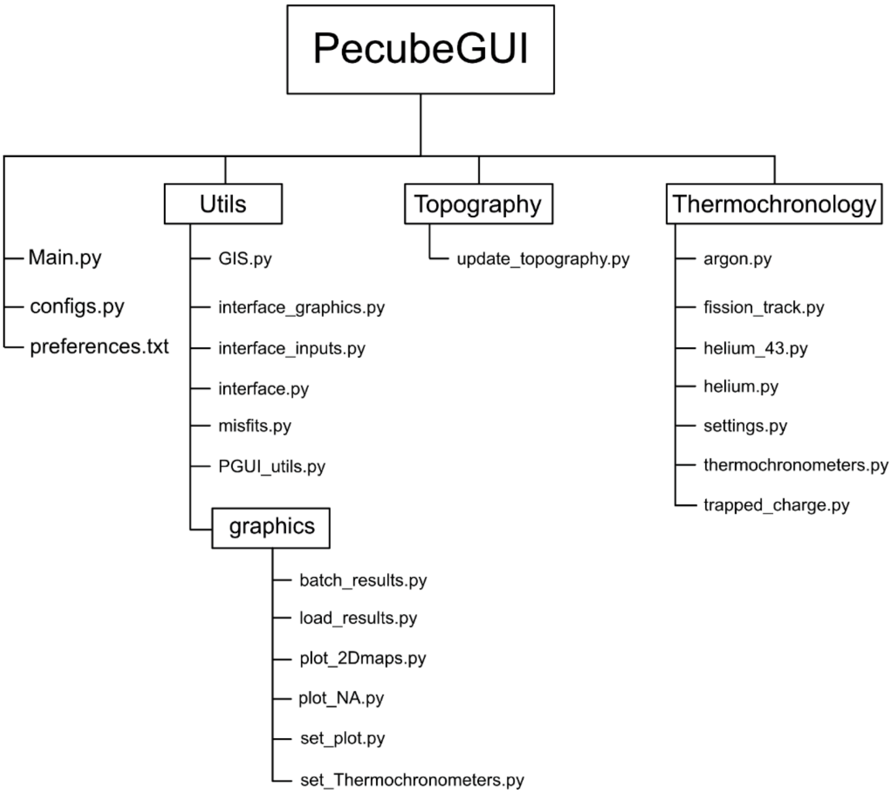

**Figure 2**. Structure of the PecubeGUI python libraries. The interface is split into three main libraries: Utils, Topography, and Thermochronology, which each focus on specific themes (see main text for more details).

The core of PecubeGUI consists of three python files: *Main.py*, *configs.py*, *and preferences.txt* (Fig. 2). The *Main.py* file launches the interface and defines the main functionalities of the welcome window. The *configs.py* file contains all default Pecube parameters together with their associated input labels, while *preferences.txt* stores user-defined settings that control the appearance and behaviour of the interface. Other sections of the interface are grouped into three main libraries: Utils, Topography, and Thermochronology. The *Utils* library contains all Python modules that control generic interface behaviour, including the organisation of tabs, tables, and input fields. The *Topography* library contains the routines used to load and configure the topographic evolution scenarios. Finally, the *Thermochronology* library includes all modules related to the thermochronometric inputs, organised by thermochronometric system (Ar/Ar, fission-track, $^4$He/$^3$He, (U-Th)/He, trapped charge). Each system-specific module can handle one or more mineral species (e.g., apatite and zircon (U-Th)/He).

We present some of the new PecubeGUI functionalities in Sect. 3 below. An online user manual for PecubeGUI is available (Bernard, 2026) and we invite users to refer to this documentation for more details about PecubeGUI usage.

## 2.4 CalcAge and updated thermochronometric systems

The external program CalcAge is implemented in Fortran90 and enables users to calculate thermochronometry data after a Pecube run without rerunning the full thermal-kinematic model. This functionality is particularly useful when modifying kinetic parameters or radiation-damage models, as it significantly reduces computation time. As inputs, CalcAge takes the cooling histories predicted by Pecube for each sample location, together with the user-defined kinetic parameters specified through the interface. Communication between PecubeGUI and CalcAge is handled via the text file “Sample-specific.txt”, which provides all necessary sample information and associated kinetic values. Following execution, CalcAge outputs thermochronometry data predictions to a series of CSV files generated in the “output” directory of the active Pecube project, as is the case in Pecube version 4.2. PecubeGUI then reads these outputs to generate model-data comparison plots and visualizations (see Sect. 3.2, Bernard, 2026).

### 2.4.1. Radiation damages and helium production-diffusion model

The development of PecubeGUI has been accompanied by the integration of an updated production-diffusion (PD) model for (U-Th)/He thermochronometry, based on the formulation of Guenthner (2021). This PD subroutine is shared between Pecube and CalcAge (Fig. 1) and computes the spatial and temporal accumulation of $^4$He along the radius of a spherical grain at each time step. The model incorporates alpha-ejection corrections (Ft factor) for $^{238}$U, $^{235}$U, and $^{232}$Th, following the approach of Ketcham (2005). For a radial position subject to alpha-ejection effects, $^4$He production is calculated as:

$$^4He_i = 8\,^{238}U_i Ft_{238}\left(e^{\lambda_{238}t_2} - e^{\lambda_{238}t_1}\right) + 7\,^{235}U_i Ft_{235}\left(e^{\lambda_{235}t_2} - e^{\lambda_{235}t_1}\right) + 6\,^{232}Th_i Ft_{232}\left(e^{\lambda_{232}t_2} - e^{\lambda_{232}t_1}\right), \quad (2)$$

where $\lambda_{238}$, $\lambda_{235}$, $\lambda_{232}$, and $Ft_{238}$, $Ft_{235}$, $Ft_{232}$ are the decay rate constants and the Ft correction factors for $^{238}$U, $^{235}$U and $^{232}$Th, respectively, and $t_2$ and $t_1$ are the times bounding the timestep for the calculation. For a radial position away from the alpha ejection effect, the Ft factor values are set to one.

Next, the model solves the 1D diffusion equation using the finite-difference method. The He-diffusion equation for a sphere is (Carslaw and Jaeger, 1959):

https://doi.org/10.5194/egusphere-2026-2286
Preprint. Discussion started: 28 May 2026

$$\frac{\partial^4 He}{\partial t} = \frac{D}{r^2}\frac{\partial}{\partial r}\left(r^2 \frac{\partial^4 He}{\partial r}\right) + P, \qquad (3)$$

where *D* is chemical diffusivity of Helium, *r* is the radial position, and *P* is the production rate of $^4$He (eq. 2). The main contribution of this work is the implementation in Pecube of diffusion models that account for radiation-damage effects on $^4$He mobility in apatite and zircon (Flowers et al, 2009; Gautheron et al., 2009; Guenthner et al., 2013; Willett et al., 2017). Because helium diffusivity *D* varies as a function of the time-temperature path, *D* is calculated for all time steps prior to solving the $^4$He diffusion equation following approaches detailed in the above references. Once the spatial distribution of $^4$He is obtained, the total $^4$He retained within the grain is computed using Romberg integration, and the corresponding (U-Th)/He age is determined through an iterative procedure (Fig. 3).

The iterative algorithm begins by defining initial lower and upper bounds on the age, corresponding to the minimum and maximum time of the thermal history. An initial age estimate ($t_{mid}$, Fig. 3) is then set to the midpoint of these bounds, and the associated $^4$He concentration is calculated. The age bounds are then updated accordingly, and the iteration continues until the residual of the difference of the age limits is below a threshold value ($t_c = 10^{-4}$ Myr; Fig. 3).

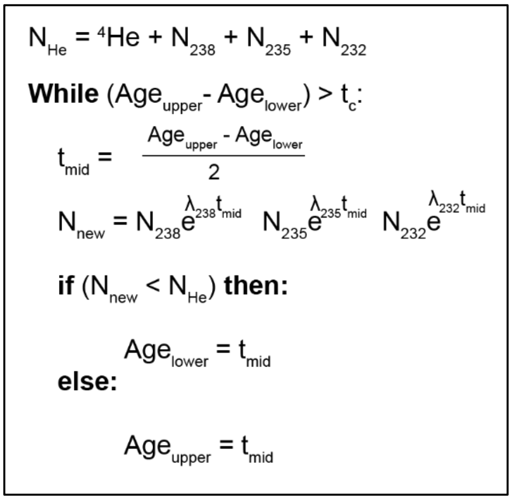

```
$N_{He} = {}^4He + N_{238} + N_{235} + N_{232}$
While $(Age_{upper} - Age_{lower}) > t_c$:
    $t_{mid} = \frac{Age_{upper} - Age_{lower}}{2}$
    $N_{new} = N_{238}e^{\lambda_{238}t_{mid}}\ N_{235}e^{\lambda_{235}t_{mid}}\ N_{232}e^{\lambda_{232}t_{mid}}$
    if $(N_{new} < N_{He})$ then:
        $Age_{lower} = t_{mid}$
    else:
        $Age_{upper} = t_{mid}$
```

**Figure3.** Iterative procedure to compute a (U-Th)/He age according to the amount of $^4$He after solving for diffusion. $N_{238}$, $N_{235}$, and $N_{232}$ are the amount of parent isotope corrected for alpha ejection for $^{238}$U, $^{235}$U, $^{232}$Th respectively. $Age_{upper}$ and $Age_{lower}$ are the upper and lower limits for the age, taken as the time limits of the thermal history at the start of the iterative loop. The iteration runs until the difference of the age limits reach a value below the threshold value tc. We define $t_c$ equal to $10^{-4}$ Myr. See the main text for a description of the iterative procedure.

When predictions are made on all surface model nodes, users provide a single set of kinetic parameter values for each thermochronometric system. In inverse modelling, the user provides grain-specific kinetics via PecubeGUI that include grain radius, uranium and thorium concentration (ppm), and radiation damage annealing kinetics (e.g., rmr0).

### 2.4.2. Apatite $^4$He/$^3$He thermochronometry

Apatite $^4$He/$^3$He spectra can be provided and modelled within the new Pecube version (v.4.3). The heating schedule for the $^4$He/$^3$He degassing experiment can be provided for each sample or left as the default schedule. The algorithm first calculates $^4$He production and diffusion from the modelled geological thermal history. The resulting $^4$He concentration profile along the grain radius is then used as the initial state for modelling the release of $^4$He and synthetic $^3$He in a degassing experiment. $^4$He/$^3$He spectra are predicted for each heating step provided (i.e., cumulative release of $^3$He, $\Sigma F^3$He). In inverse modelling mode, the misfit function that compares predictions with observations for $^4$He/$^3$He thermochronometry follows the L1-norm:

$$\Phi_{4He/3He} = \sum_{i=1}^{N_{obs}} \sum_{j=1}^{N_{step}} \left( \frac{\left| S_{j,i}^{obs} - S_{j,i}^{pred} \right|}{\sigma_{j,i}} \right), \qquad (4)$$

where $N_{obs}$ and $N_{step}$ are the number of observed $^4$He/$^3$He spectra and the number of heating steps for each spectrum, $S_{j,i}^{obs}$ and $S_{j,i}^{pred}$ are the observed and predicted released $^4$He/$^3$He ratio ($R_{step}/R_{bulk}$) for heating step *i* in release spectrum *j*. For all other thermochronometers, the misfit function can be chosen from a list of available functions and include the chi-squared, the reduced chi-squared, or the L2-norm function (see Bernard, 2026; for more details).

### 2.4.2. Apatite fission-track annealing

The new version of Pecube (v4.3) also incorporates the improved fission-track annealing model for apatite developed by Ketcham et al. (2007). This model enables predicting fission-track annealing for a wide range of apatite varieties using proxies such as composition (Cl content), dimensions of etch-figures (Dpar) and the generic factor rmr0 (the "reduced length of the more-resistant apatite at the time-temperature conditions where the reduced length of the less-resistant apatite falls to zero"; Ketcham, 2005). The algorithm to calculate fission-track annealing follows Ketcham et al. (2007).

## 3. Highlights of the new interface

Here, we describe some of the key functionalities of PecubeGUI, which aim to help users provide and validate their input parameters.

https://doi.org/10.5194/egusphere-2026-2286
Preprint. Discussion started: 28 May 2026

## 3.1 Input parameters

### 3.1.1 Loading and visualising topography from a DEM

A key feature of Pecube is its ability to incorporate prescribed topographic evolution scenarios as surface boundary conditions. In previous versions of the code, topography was provided as a single-column text file of elevations, either made by the user or extracted from a ~900 m resolution Digital Elevation Model (DEM) of global topography.

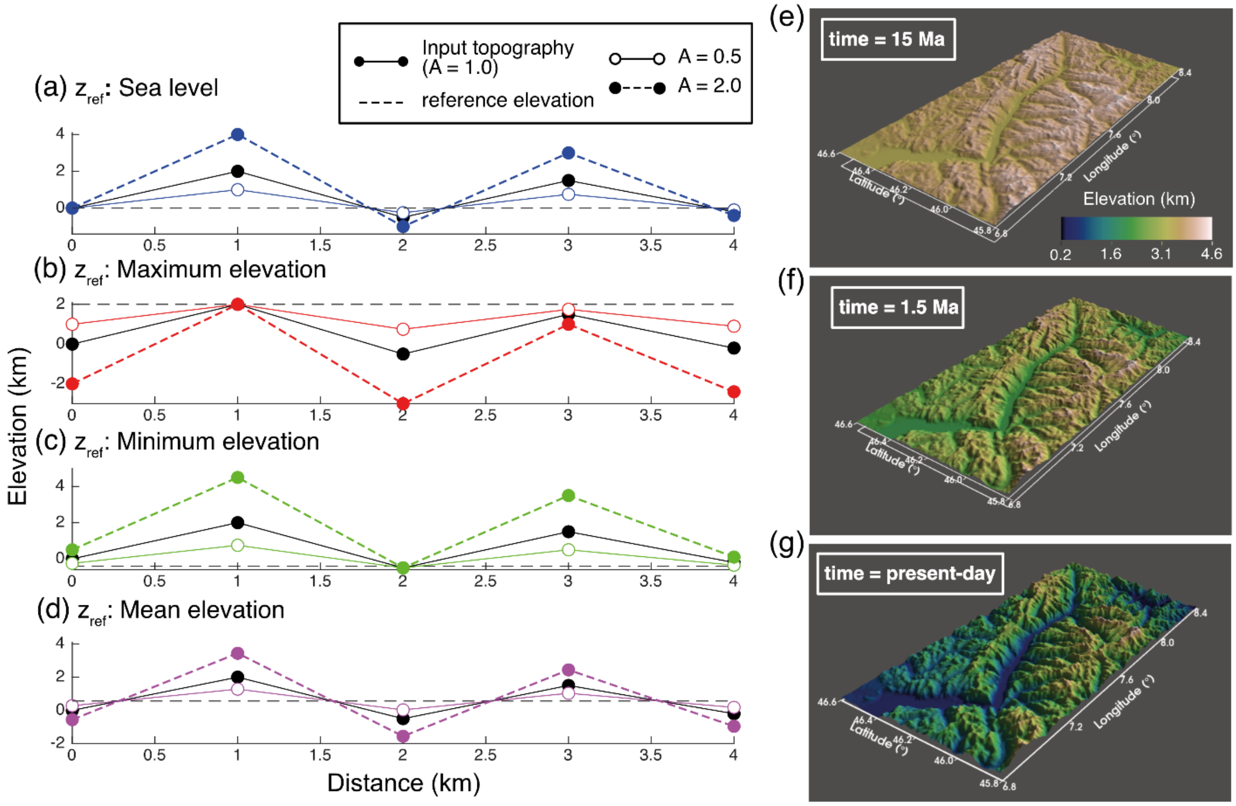

**Figure 4.** Example of a topographic evolution scenario as described and visualised in PecubeGUI. (a-d) Topographic profiles with prescribed relief amplification (A, eq. 6) for each reference elevation ($z_{ref}$, eq. 6) available in PecubeGUI. In (e-g) the DEM represents part of the Rhone valley catchment in the Swiss Alps. The topographic evolution scenario considers a relief amplification of 30 % at 15 Ma (e) and 60 % at 1.5 Ma (f) of the modern topography (g), through valley lowering ($z_{ref} = z_{max}$). DEM from NASA Shuttle Radar Topography Mission (SRTM, 2013).

However, this file is large (~3 GB) and impractical to store or distribute. To overcome these limitations, PecubeGUI implements an interactive workflow for extracting and loading topography into Pecube. Using the *gdal v3.9.3* and bmi-topography v0.8.5 (Piper and Hutton, 2024) Python packages, the interface downloads DEM tiles in GeoTIFF format from the OpenTopography platform. Given the coordinates of the lower-left corner of the user's region of interest (ROI), the desired spatial resolution (dlat and dlon in Pecube), and model grid dimensions (nx and ny in Pecube), the corresponding DEM is downloaded from the 90-m Shuttle Radar Topography Mission dataset (SRTMGL$_3$, NASA 2013). This procedure eliminates the need to store large DEM files locally and provides immediate access to high-quality topography data. Any loaded DEM can be visualised interactively in 3D though the PyVista v0.45.0 Python package (Sullivan and Kaszynski, 2025).

Pecube describes topographic evolution at each surface node as:

$$z_i = Az_0 + \Delta z, \tag{5}$$

where $A$ and $\Delta z$ are amplification and vertical offset parameters, and $z_0$ the input (present-day) elevation. In this formulation, the implicit reference elevation for scaling topographic relief by $A$ is sea-level ($z = 0$ m).

To expand the range of possible topographic evolution scenarios, we modified eq. (5) to incorporate an explicit reference elevation:

$$z_i = z_{ref} - \left(A * \left(z_{ref} - z_0\right)\right) + \Delta z, \tag{6}$$

where $z_{ref}$ is the elevation from which $A$ is applied. This new formulation enables the implementation of topographic evolution scenarios referenced to a custom DEM elevation (Fig. 4a-d). For example, setting up $z_{ref}$ to the maximum DEM elevation focuses topographic evolution on the valleys (in particular, A < 1 models valley incision; Fig. 4b), while setting $z_{ref}$ to the minimum DEM elevation focuses topographic evolution on summit areas (with A > 1 modelling relief decrease through focused summit lowering; Fig. 4c).

A very useful feature of PecubeGUI is that it allows the input topographic evolution scenario to be visualised, so that the user can check whether it is parameterised correctly before starting the model run. An example evolution scenario generated within PecubeGUI is shown in Figure 4. The topographic evolution of the Rhone valley catchment (Swiss Alps) is simulated using three stages. At 15 Ma, topographic relief is set to 30 % of its modern value ($A$ = 0.3, eq. 6, Fig. 4e), using the maximum modern elevation of the DEM as $z_{ref}$. This setup implies that relief increase occurs through valley deepening. Relief then increases linearly, reaching 60 % of modern relief at 1.5 Ma ($A$ = 0.6, eq. 6, Fig. 4f). From 1.5 Ma to the present, an increase in valley incision rate yields the modern relief ($A$ = 1.0, eq. 6, Fig. 4g) corresponding to a ~66 % increase in relief over the last 1.5 Ma (e.g., Valla et al., 2012).

### 3.1.2. Pecube thermal parameters and 1D geotherm visualisation

Setting up Pecube models requires specifying the thermal parameters used to solve the 3D heat-transport equation (eq. 1). In Pecube v4.2, these parameters include crustal thickness ($H_c$), basal temperature ($T_b$), thermal diffusivity ($\kappa$), and radiogenic heat-production rate ($H_p$). To assist users in evaluating their chosen parameter values, PecubeGUI provides a graphical panel on the right-hand side of the main window displaying the corresponding 1D steady-state geotherm (Fig. 5). Following Reiners and Brandon (2006), two different 1D thermal solutions are used depending on the Peclet number $P_e = \frac{\dot{\varepsilon} z_b}{\kappa}$, where $\dot{\varepsilon}$ is the erosion rate and $z_b$ the basal depth (equivalent to H$_c$). For high erosion rates, advection dominates heat transport, $P_e > 1$, and the temperature at depth z is given by:

$$T(z) = \left(T_b - T_s + \frac{H_p z_b}{\dot{\varepsilon}}\right) \frac{1 - \exp\left(-\frac{\dot{\varepsilon} z}{\kappa}\right)}{1 - \exp\left(-\frac{\dot{\varepsilon} z_b}{\kappa}\right)} - \frac{H_p z}{\dot{\varepsilon}} + T_s, \qquad (7a)$$

260 whereas for $P_e < 1$, when diffusion dominates, the solution simplifies to:

$$T(z) = \frac{(T_b - T_s) z}{z_b} + \frac{H_p z (z_b - z)}{\dot{\varepsilon}} + T_s, \qquad (7b)$$

with $T_s$ the surface temperature.

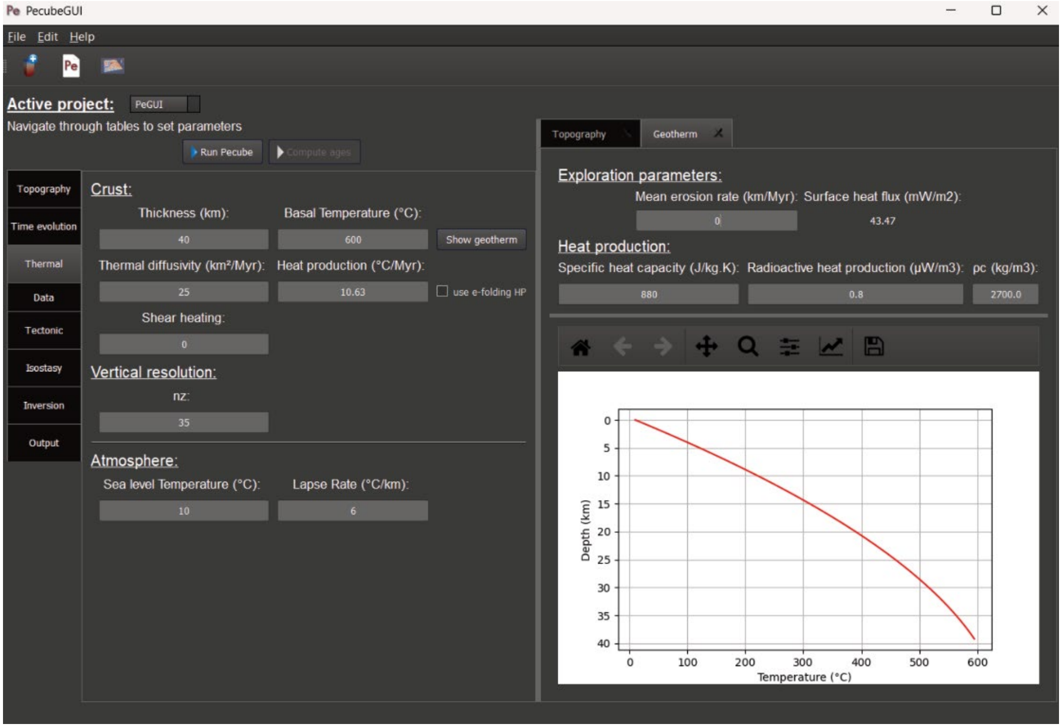

Crust:
Thickness (km): 40
Basal Temperature (°C): 600
Thermal diffusivity (km²/Myr): 25
Heat production (°C/Myr): 10.63
Shear heating: 0

Vertical resolution:
nz: 35

Atmosphere:
Sea level Temperature (°C): 10
Lapse Rate (°C/km): 6

Exploration parameters:
Mean erosion rate (km/Myr): 0
Surface heat flux (mW/m2): 43.47

Heat production:
Specific heat capacity (J/kg.K): 880
Radioactive heat production (µW/m3): 0.8
ρc (kg/m3): 2700.0

**Figure 5.** Example visualisation of input 1D geotherm in PecubeGUI (right-hand side) according to the thermal parameter values provided to Pecube (left-hand side). Corresponding rock properties ($R$, $c$, $\rho_c$) are indicated in the top right panel and can be modified, leading to automatic recalculation of the Pecube input parameters. The mean erosion rate factor is only here for visualisation purposes, i.e., to explore the impact of erosion rate on the 1D geotherm, but has no impact on the Pecube calculation.

In Pecube, the heat-production rate must be supplied in units of °C Myr$^{-1}$, yet thermal data is more commonly expressed in terms of rock properties such as specific heat capacity ($c$; J kg$^{-1}$ K $^{-1}$,), radiogenic heat production ($R$; µW m$^{-3}$), and surface 265 heat flux (mW m$^{-2}$). To accommodate this, PecubeGUI accepts a broader range of thermal input parameters and converts them automatically to a heat-production rate in °C Myr$^{-1}$ for Pecube (Fig. 5). This conversion is performed as:

$$H_p\left[\frac{°C}{Myr}\right] = H_p\left[\frac{°C}{s}\right] S = \frac{R\left[\frac{W}{m^3}\right]}{\rho_c\left[\frac{kg}{m^3}\right] * c\left[\frac{J}{kgK}\right]} S, \qquad (8)$$

Where $\rho_c$ is crustal density and $S$ is a multiplication factor to convert seconds to Myr.

In Pecube v4.2, the heat production rate is assumed uniform with depth. In the new version Pecube v4.3, the heat-production rate can now be defined as depth-dependent; $H_p = H_p(z)$, following an exponential decrease:

$$H_p(z) = H_{p,0} e^{-z/z_e}, \tag{8}$$

where $H_{p,0}$ is the heat-production rate at the surface and $z_e$ is the e-folding depth, at which $H_p$ has decreased to a value of $1/eH_{p,0}$.

### 3.1.3 Visualising input fault geometry and kinematics

Since the last major update of Pecube (Braun et al., 2012), rock advection across fault-bounded domains can be prescribed. Although users may define multiple faults with a wide range of geometries, the implementation requires all faults to share a common strike, that is, all faults must be mutually parallel. Fault geometry is specified by a series of user-defined nodes connected by straight segments, forming a 2D planar surface (see Braun et al., 2012, for more details).

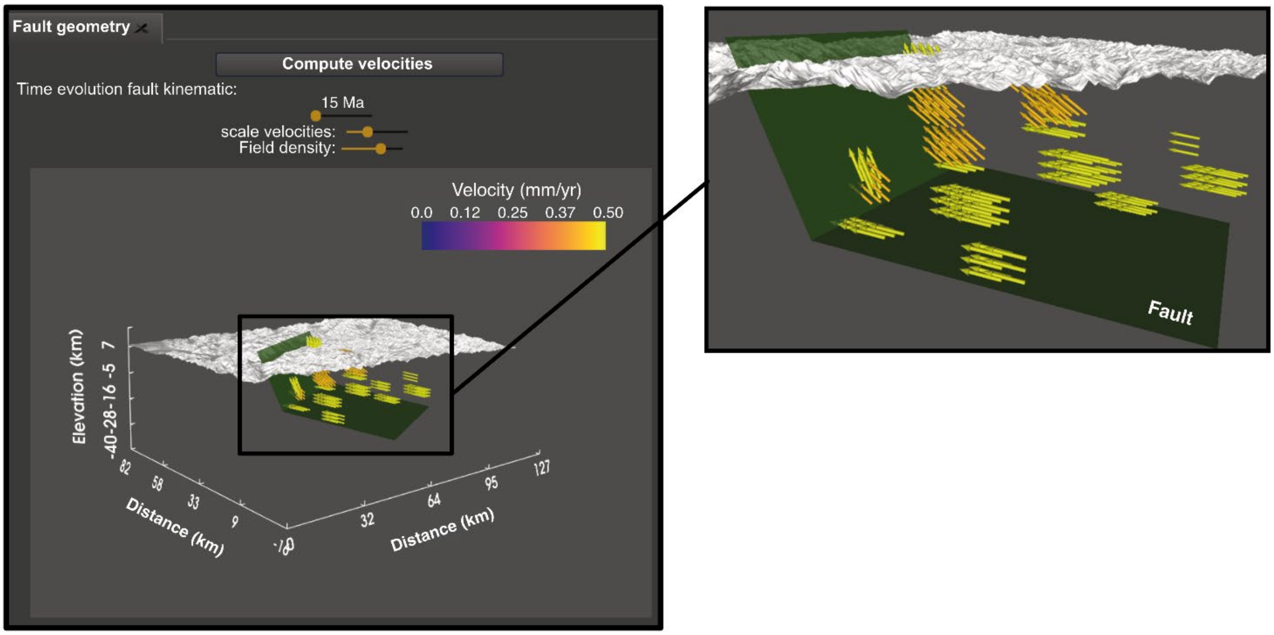

**Figure 6.** Example of input fault kinematics visualised in PecubeGUI. A flat-ramp thrust fault is defined with three nodes, and the velocity field is shown for an input 0.5 km Myr$^{-1}$ slip rate along the fault. Note the variation of velocity at the junction of two fault segments to ensure mass conservation (see Braun et al., 2012 for more details).

The kinematic history of each fault is defined through a sequence of time intervals, each associated with a prescribed slip rate. Slip is applied parallel to each fault segment, and Pecube computes the mean velocity between two adjacent segments to ensure mass conservation. Positive slip rates correspond to normal faulting, whereas negative rates define thrust faults. The ordering of fault nodes also determines the moving block, conventionally taken as the block on the right-hand side of the fault (see Braun et al., 2012).

Parameterising and verifying fault geometry and kinematics usually requires running Pecube test simulations and inspecting the resulting VTK output files in an external visualisation software (e.g., Paraview, Ahrens et al., 2005), rendering the setup process laborious. PecubeGUI now integrates a 3D visualisation tool (PyVista, Sullivan and Kaszynski, 2025) enabling inspection of input fault geometry and kinematic history prior to a model run. After defining fault geometry and kinematics in dedicated tables, users can visualise the resulting kinematic evolution interactively within PecubeGUI using a time-dependent slider (Fig. 6), greatly simplifying model setup and validation.

### 3.1.4 Providing sample and grain-specific kinetic information

Thermochronometry predictions in Pecube can be generated either at all surface nodes of the input topography or at specific sample locations. In Pecube v4.2, sample-specific coordinates (latitude, longitude and elevation), together with additional information about the thermochronometer systems to be modelled (e.g., AHe, AFT, ZHe), must be supplied manually via a CSV file. In PecubeGUI, this process is simplified and all sample information is provided directly into dedicated, interactive tables. Users first provide sample locations, which can be visually checked before running a Pecube model through a 2D map of the input topography overlaid with sample locations (Fig. 7). For each location, users may specify the number of observations (e.g., single-grain (U-Th)/He dates, fission-track data, $^4$He/$^3$He degassing spectra) associated with each thermochronometer (i.e., AHe, AFT, ZHe, etc.). Next, PecubeGUI allows users to input kinetic parameter values for each individual observation (thermochronometric system or grain). The updated Pecube version (v4.3) released with this contribution incorporates advanced diffusion and annealing models not included in Pecube v4.2. Each thermochronometer has its own set of kinetic parameters, all of which can be provided via structured, interactive tables.

Figure 7 illustrates this for the apatite (U-Th)/He system. Users can select among several helium-diffusion models (Farley et al., 2000; Flowers et al., 2009; Gautheron et al., 2009; Shuster et al., 2006; Willett et al., 2017) and alpha-ejection corrections (Farley et al., 1996; Ketcham et al., 2011). Additional required inputs are also entered in these tables, and include observed ages and uncertainties, grain sizes (expressed as equivalent-sphere radii), uranium and thorium concentrations, and radiation-damage annealing parameters (e.g., rmr0; Ketcham, 2005). Apatite $^4$He/$^3$He spectra can also be provided through the interface. The same workflow applies to all other thermochronometric systems supported by Pecube, ensuring a streamlined and coherent sample-input structure across the full range of available thermochronometers.

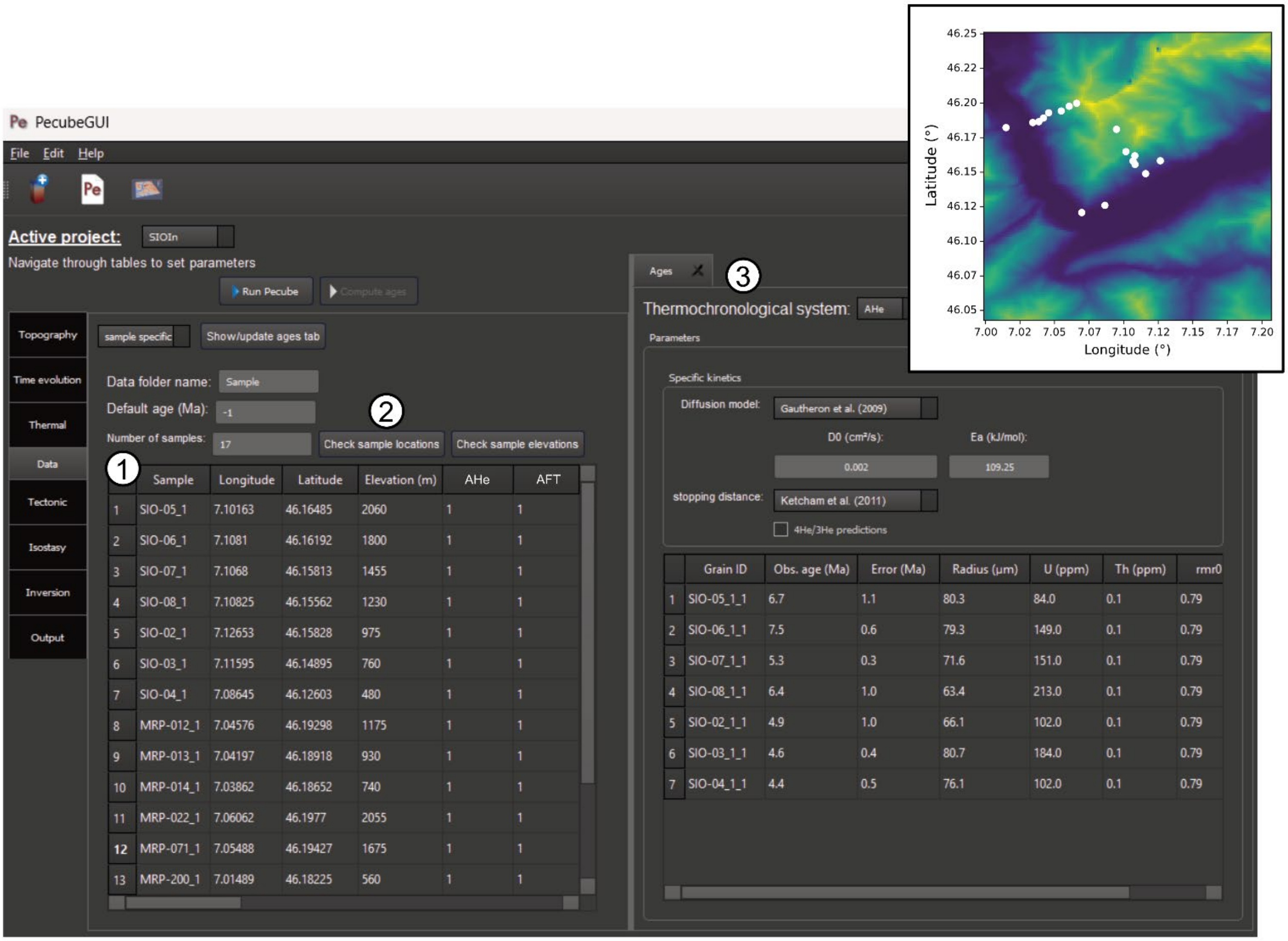

Active project: SIOIn
Navigate through tables to set parameters

sample specific

Data folder name: Sample
Default age (Ma): -1
Number of samples: 17

| | Sample | Longitude | Latitude | Elevation (m) | AHe | AFT |
|---|---|---|---|---|---|---|
| 1 | SIO-05_1 | 7.10163 | 46.16485 | 2060 | 1 | 1 |
| 2 | SIO-06_1 | 7.1081 | 46.16192 | 1800 | 1 | 1 |
| 3 | SIO-07_1 | 7.1068 | 46.15813 | 1455 | 1 | 1 |
| 4 | SIO-08_1 | 7.10825 | 46.15562 | 1230 | 1 | 1 |
| 5 | SIO-02_1 | 7.12653 | 46.15828 | 975 | 1 | 1 |
| 6 | SIO-03_1 | 7.11595 | 46.14895 | 760 | 1 | 1 |
| 7 | SIO-04_1 | 7.08645 | 46.12603 | 480 | 1 | 1 |
| 8 | MRP-012_1 | 7.04576 | 46.19298 | 1175 | 1 | 1 |
| 9 | MRP-013_1 | 7.04197 | 46.18918 | 930 | 1 | 1 |
| 10 | MRP-014_1 | 7.03862 | 46.18652 | 740 | 1 | 1 |
| 11 | MRP-022_1 | 7.06062 | 46.1977 | 2055 | 1 | 1 |
| 12 | MRP-071_1 | 7.05488 | 46.19427 | 1675 | 1 | 1 |
| 13 | MRP-200_1 | 7.01489 | 46.18225 | 560 | 1 | 1 |

Thermochronological system: AHe

Diffusion model: Gautheron et al. (2009)
D0 (cm²/s): 0.002
Ea (kJ/mol): 109.25
stopping distance: Ketcham et al. (2011)
☐ 4He/3He predictions

| | Grain ID | Obs. age (Ma) | Error (Ma) | Radius (μm) | U (ppm) | Th (ppm) | rmr0 |
|---|---|---|---|---|---|---|---|
| 1 | SIO-05_1_1 | 6.7 | 1.1 | 80.3 | 84.0 | 0.1 | 0.79 |
| 2 | SIO-06_1_1 | 7.5 | 0.6 | 79.3 | 149.0 | 0.1 | 0.79 |
| 3 | SIO-07_1_1 | 5.3 | 0.3 | 71.6 | 151.0 | 0.1 | 0.79 |
| 4 | SIO-08_1_1 | 6.4 | 1.0 | 63.4 | 213.0 | 0.1 | 0.79 |
| 5 | SIO-02_1_1 | 4.9 | 1.0 | 66.1 | 102.0 | 0.1 | 0.79 |
| 6 | SIO-03_1_1 | 4.6 | 0.4 | 80.7 | 184.0 | 0.1 | 0.79 |
| 7 | SIO-04_1_1 | 4.4 | 0.5 | 76.1 | 102.0 | 0.1 | 0.79 |

**Figure 7.** Providing sample-specific information to PecubeGUI. Sample coordinates and the number of observations at each sample location are provided in Table (1). The locations of samples can be checked, plotted on the input topography (inset figure) by clicking button (2). Kinetic parameter values and helium-diffusion model selection are shown in window (3) with the AHe system taken here as an example. See main text for further description.

## 3.2. Visualising and exporting Pecube model results

### 3.2.1. Conventional thermochronology plots

PecubeGUI incorporates all of the conventional plots commonly used to visualise thermochronological modelling results. These include time-temperature plots; age-elevation and age-distance relationships, age versus effective uranium (eU), and observed versus predicted ages (Fig. 8). Plot generation is handled by the pyplotPecube Python package (Robert, 2021), which is fully integrated into PecubeGUI. In addition to these standard visualisations, Pecube-specific outputs include plots of observed versus predicted sample elevations. A common practice in Pecube modelling is to down-sample the input topography to reduce computation time, which can result in a degraded DEM where model node elevations differ from field sample elevations by several hundred meters. Such discrepancies can affect the comparison between observed and modelled thermochronometer data. The observed versus predicted elevation plot provides a direct diagnostic of these differences. Each plot is associated with an interactive toolbar that allows users to modify default settings (such as marker colour, size, and shape) according to their preferences.

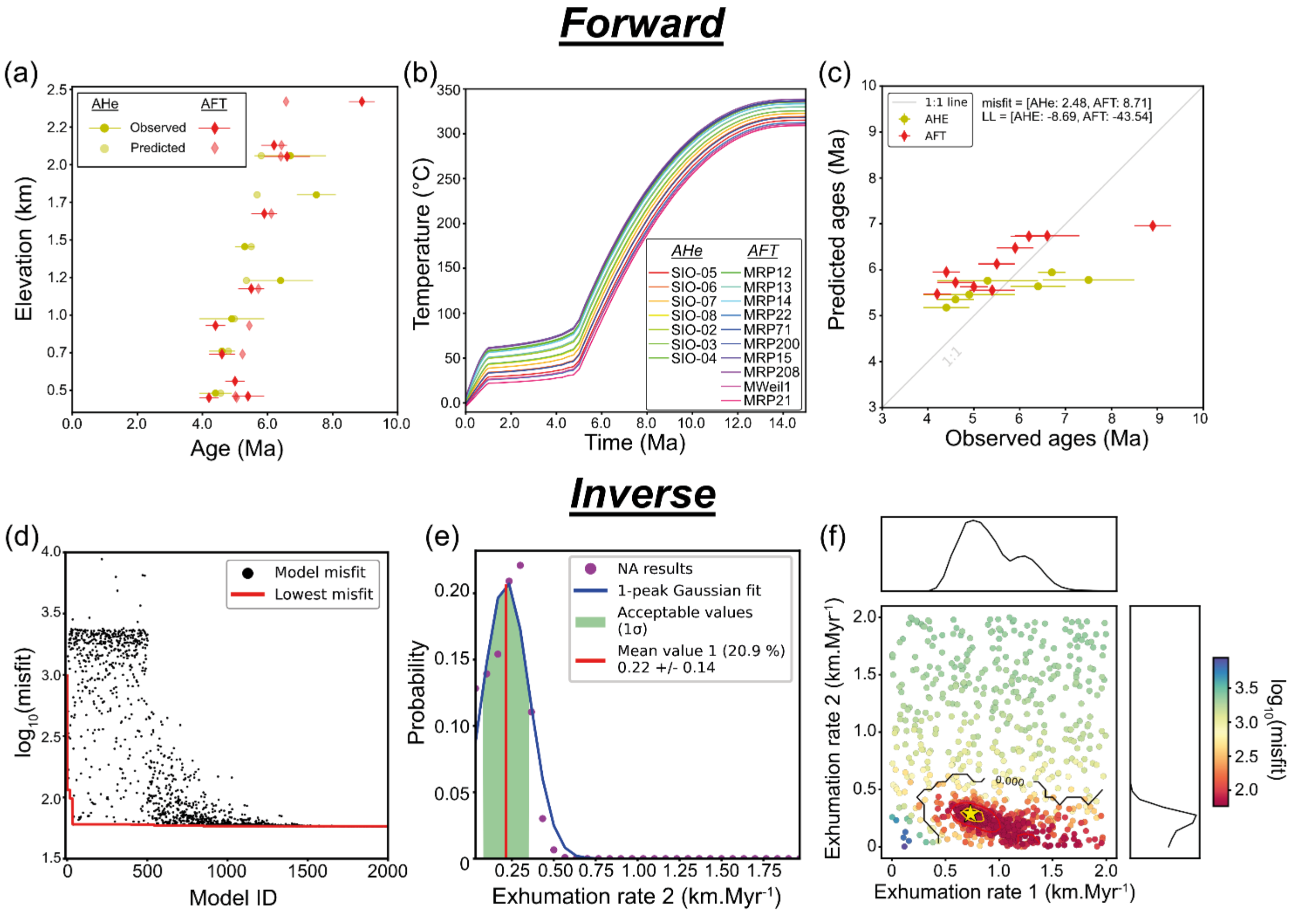

**Figure 8.** Example of plots available in PecubeGUI. In forward modelling mode, conventional plots include age-elevation relationships for observed and predicted data (a), time-temperature paths at sample locations (b), and observed versus predicted ages (c). In inverse modelling mode, plots include misfit versus model iteration (d), probability distributions of inverted parameters (e), and 2D scatter plots of misfit as a function of different inverted parameters with 1D probability distributions (f). The plots are generated using the python package pyplotPecube (Robert, 2021) included in PecubeGUI.

https://doi.org/10.5194/egusphere-2026-2286
Preprint. Discussion started: 28 May 2026

When performing inverse modelling with Pecube, additional diagnostic plots are available. These include misfit versus model iteration, 1D probability distributions of inverted parameters, and 2D scatter plots illustrating the trade-off between model 325 parameters (Fig. 8 d-f; Robert, 2021). Estimating parameter probability distributions within a Bayesian framework requires running the appraisal stage of the neighbourhood algorithm (NA, Sambridge, 1999b), which is not yet integrated into the PecubeGUI package. An alternative and external way to visualise the output of both Pecube inversions and parameter appraisal is provided by the recently released PyPIVoT (Wapenhans et al., 2025) and MATPIVoT (Gong et al., 2025) visualisation tools, developed in Python and Matlab, respectively.

### 330 3.2.2. Plotting 2D and 3D visualisations of Pecube model output

The 3D formulation of Pecube enables visualisation and analysis of the thermal field and modelled thermochronometer data through both 2D maps and 3D views. For example, users may wish to assess the spatial distribution of temperature at a given depth, inspect the geometry of isotherms beneath topography, or evaluate predicted erosion rates at the end of a model run (Fig. 9a-b).

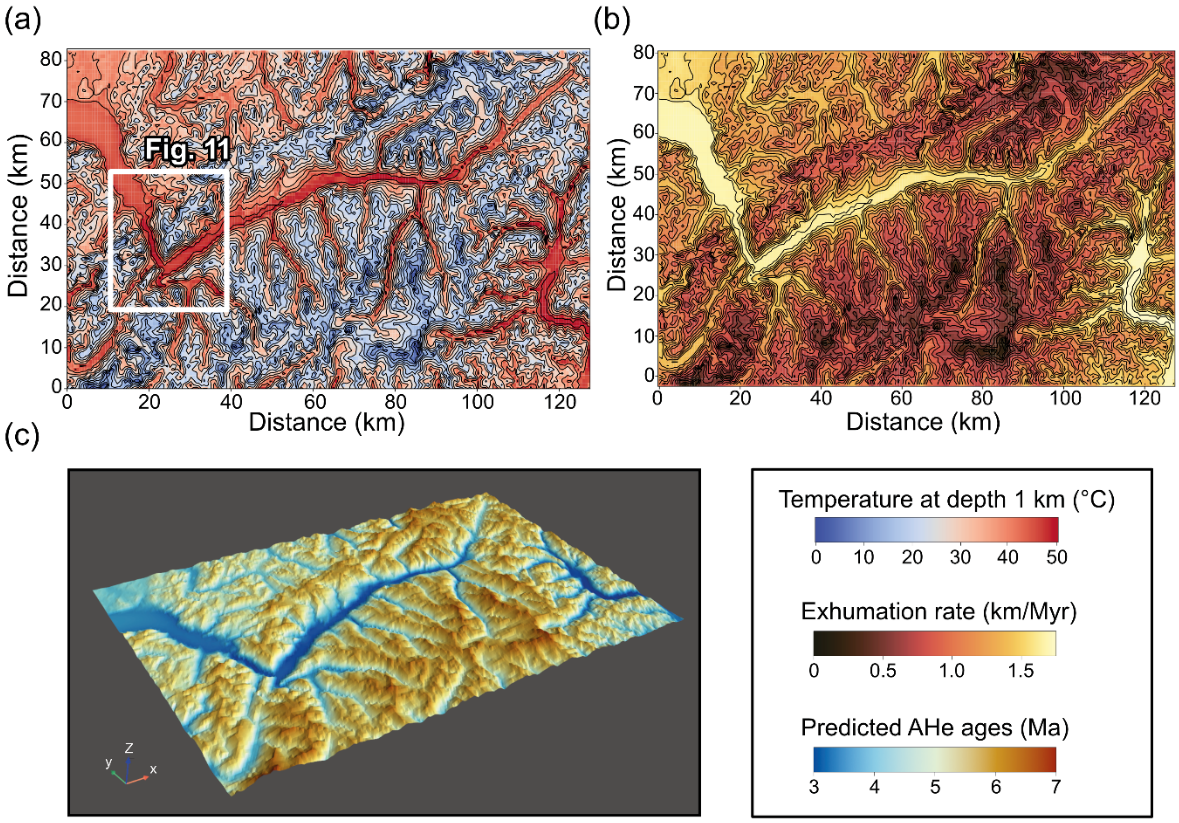

**Figure 9.** Example of 2D maps and 3D visualisation in PecubeGUI. The spatial distribution of temperature at 1 km depth and predicted exhumation rates are shown in (a) and (b), respectively, for a synthetic example of the Rhône valley

(Switzerland). An interactive 3D visualisation of spatial distribution of AHe ages is shown in (c). Box in (a) shows location of Figure 11.

Pecube outputs can also be explored as interactive 3D models within PecubeGUI, providing an intuitive way to assess relationships between thermochronometer data, depth of isotherms, fault-controlled exhumation pattern, and topographic features (Fig. 8c). The interface relies on the PyVista Python package (Sullivan and Kaszynski, 2025) to read and render the vtk files generated after each Pecube model run. This integrated visualisation capability removes the need for external software such as Paraview, and greatly facilitates the interpretation of model outputs, particularly in complex tectonic and/or geomorphic settings.

## 4. Applications and active development

### 4.1 Example of applications

#### 4.1.1. Teaching application (batch mode): the effect of topography on age-elevation relationships

We provide here an example of how PecubeGUI can be used for teaching purposes via a newly developed "batch mode", which allows efficient exploration of the impact of one parameter on predicted thermochronometer data. The "batch mode" enables the impact of a parameter on thermochronometric predictions to be explored by generating a set of Pecube models, with a range of prescribed values for the targeted parameter, within a single project.

Thermochronology studies generally aim to resolve the exhumation history of a study area. This can be done, for instance, by collecting and analysing samples along altitudinal profiles and interpretation of the resulting age-elevation relationships. However, this analysis commonly assumes that the closure isotherms of the relevant thermochronometric systems are horizontal, whereas in reality these are perturbed by the topography, leading to bias in the exhumation rate inferred from an age-elevation plot. The magnitude of this perturbation depends mainly on the topographic wavelength and amplitude (Braun, 2002). In this example, we use the "batch mode" functionality to explore the role of topographic relief in impacting the slope of the age-elevation relationship (i.e., the apparent exhumation rate, $\dot{E}_{app}$ or AER).

We design a 100x50 km synthetic sinusoidal topography using a built-in tool of PecubeGUI (Bernard, 2026) with a wavelength of 50 km, and a present-day topographic amplitude of 2 km (Fig. 10a). We consider 4 models that start with different initial topographic relief, by providing a range of relief amplification values from 0 to 3 times the final topographic relief of 2 km (i.e., $A = 0 - 3$, $z_{ref} = \bar{z} = 935.7$ m, $\Delta z = 1$ km; eq. 5). All models assume steady-state topography from 50 Ma to 3 Ma, followed by relief change to the present-day configuration. For each model, we assume a constant rock-uplift rate of 0.3 km Myr$^{-1}$ during the 50-Myr model run. We assume an initial geotherm of about 30 °C km$^{-1}$ (basal temperature of 650°C) and consider a temperature at sea-level of 15°C with an atmospheric lapse rate of 6 °C km$^{-1}$. All other parameters are set to their default values. Finally, we compute age-elevation relationships for a series of synthetic samples along a transect perpendicular to the direction of the main valleys (Fig. 10a), for which we predict AHe, AFT, and ZHe ages using the kinetic parameters of Farley et al. (2000), Ketcham et al. (2007) and Reiners et al. (2004), respectively.

https://doi.org/10.5194/egusphere-2026-2286
Preprint. Discussion started: 28 May 2026

Results show that most of the apparent exhumation rates ($\dot{E}_{\mathrm{app}}$) overestimate the input rock-uplift rate of 0.3 km Myr$^{-1}$ for the three thermochronometers (Fig. 10b). Only models considering an increase in relief from 3 Ma to present-day (i.e., 0A$_0$; Fig. 10b) result in an AER consistent with the input rock-uplift rate for the three thermochronometers. This is because all thermochronometers crossed their closure isotherm before 3 Ma, when the topography and all isotherms were flat. Considering steady-state topography during the 50 Ma history (i.e., 1A$_0$; Figure 10b) leads to an overestimation of the true exhumation rate for all three thermochronometers, although the discrepancy decreases for higher-temperature thermochronometers ($\dot{E}_{\mathrm{app,AHe}}$ = 0.67 km Myr$^{-1}$; $\dot{E}_{\mathrm{app,AFT}}$ = 0.51 km Myr$^{-1}$; $\dot{E}_{\mathrm{app,ZHe}}$= 0.40 km Myr$^{-1}$; Fig. 10b). The overestimation of exhumation rate from the slope of the age-elevation relationship of low-temperature thermochronometers is a direct consequence of the perturbation of isotherms below the topography, which decreases exponentially with depth (Braun, 2002).

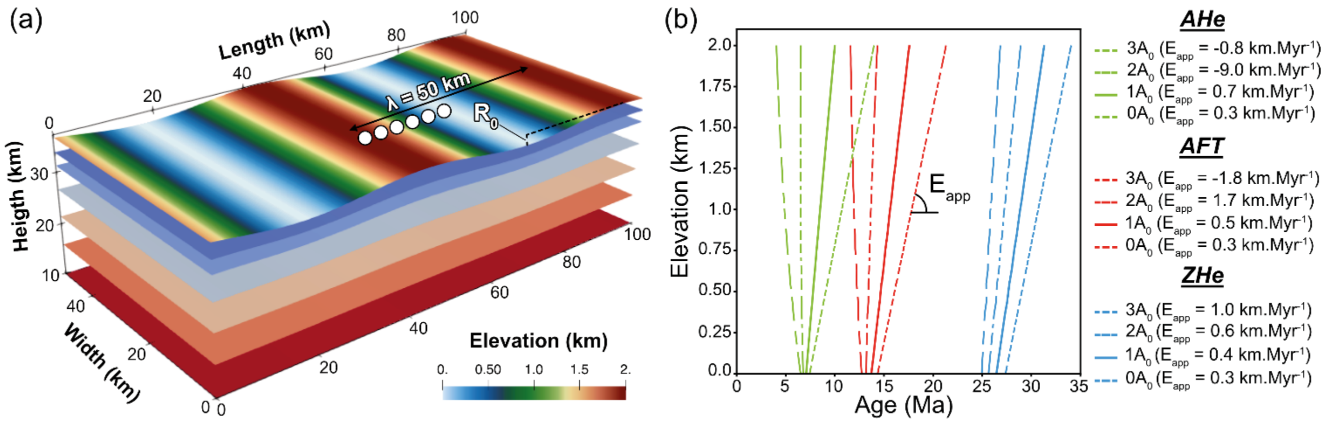

**Figure 10.** Role of topographic relief on age-elevation relationships. The synthetic sinusoidal topography is shown in (a) along with the synthetic samples (white circles) and depths of the 60, 110, 200, 300, 400 and 500°C isotherms; predicted age-elevation relationships are shown in (b) for each topographic evolution scenario and thermochronometer. Parameters A$_0$ and $\dot{E}_{\mathrm{app}}$ refer to the initial relief amplification (i.e., at time = 0; eq. 6) and apparent exhumation rate, respectively.

Finally, a significant decrease of relief (3A$_0$, Fig. 10b) reverses the age-elevation profile for the lower-temperature thermochronometers (AHe and AFT); i.e., ages on the summits are younger than those at the valley bottoms. This effect has been described by Braun (2002) and is a consequence of focused erosion on the summits due to the specific relief-decrease scenario. However, reversal of the age-elevation relationship is highly dependent on two main factors: the topographic wavelength and the background exhumation rate. The larger the topographic wavelength, the easier it is to reverse the age-elevation profile following relief decrease. Longer-wavelength topography perturbs isotherms more strongly and more deeply, so that reduction of long-wavelength topography also leads to a stronger reduction of the distance between closure depths and the surface beneath summits (Braun et al., 2002). Second, rapid exhumation rates preceding relief decrease enhances the reversal of age-elevation relationships because the age-elevation profile in the absence of relief reduction is already steep

(Olivetti et al., 2016). Third, the rate of relief change must be at least 2-3 times higher than the background exhumation rate to be recorded by the AFT and AHe systems, due to the depth of their closure isotherm (70-110°C, Valla et al., 2010).

### 4.1.2. Case study: constraining the timing and magnitude of glacial valley incision using $^4$He/$^3$He thermochronometry

The implementation of apatite $^4$He/$^3$He thermochronometry in Pecube allows the range of geological problems that can be addressed to be expanded. $^4$He/$^3$He thermochronometry exploits the spatial distribution of radiogenic $^4$He within individual apatite crystals; this distribution directly reflects the cooling history the sample experienced between the AHe closure temperature and the surface, thus providing additional constraints beyond conventional bulk AHe measurements. Consequently, $^4$He/$^3$He thermochronometry has been applied to refine the timing, magnitude and spatial propagation of both fluvial (Schildgen et al., 2010; Tremblay et al., 2015), and glacial (Shuster et al., 2011; Valla et al., 2011; 2012) valley incision. As an example, we reproduce the results of Valla et al. (2012) who investigated the timing and magnitude of glacial incision of the Rhône valley (Switzerland). In their study, Pecube inversions of apatite (U-Th)/He (AHe) and fission-track (AFT) data constrained the post-Miocene exhumation history of the region, while HeFTy modelling of apatite $^4$He/$^3$He spectra provided insight into spatially variable Quaternary exhumation through valley incision. Although conventional AHe data alone do not resolve the Quaternary relief history, the addition of $^4$He/$^3$He spectra revealed an 80-100 % increase in valley relief over the last 1.0±0.5 Ma. This timing coincides with the mid-Pleistocene transition, during which glacial-cycle periodicities increased from 40 kyr to 100 kyr while glacial-cycle amplitude increased (e.g., Herbert, 2023), leading Valla et al. (2011) to propose that glacial erosion incised the Rhône valley by 1-1.5 km since that interval.

This scenario is reproduced using the updated version of Pecube for the region of Sion (Fig. 7 inset), where 1 km of valley incision since 1.5 Ma is inferred, following a phase of rapid regional exhumation between 15 and 5 Ma and a period of tectonic quiescence thereafter (Valla et al., 2012). Predicted $^4$He/$^3$He spectra were generated for two samples, a valley-bottom sample (SIO-04, Fig. 11c) and an upper-slope sample (SIO-06, Fig. 11c) and compared with observed spectra (Fig. 11a-b). The resulting model reproduces the measured $^4$He/$^3$He profiles with high fidelity, demonstrating the potential of $^4$He/$^3$He thermochronometry to improve the resolution of modelled thermal histories. In particular, the more diffusive $^4$He/$^3$He profile observed in sample SIO-04 ($R_{step}/R_{bulk} < 0.2$ for $\Sigma F^3He < 0.1$, Fig. 11a) requires that this sample remained near the helium partial-retention zone for a longer time than sample SIO-06 (where $R_{step}/R_{bulk} > 0.2$ for $\Sigma F^3He < 0.1$, Fig. 11b). These differences indicate that the valley-bottom sample experienced a distinct cooling path relative to the summit sample (Fig. 11a-b inset), consistent with differential exhumation driven by Quaternary glacial incision.

To further illustrate the improvement in temporal resolution gained from incorporating $^4$He/$^3$He data, we convert the $^4$He/$^3$He spectrum into age profile following Shuster et al. (2004) and calculate an Increased Resolution Power (IRP) ratio defined as the difference between the $^4$He/$^3$He "edge age" ($A_{edge}$; defined as the mean age for degassing steps with $\Sigma F^3He \leq 0.1$) and the bulk AHe age ($A_{bulk}$):

$$IRP = 1 - \frac{A_{edge}}{A_{bulk}}. \tag{9}$$

In this example, the greatest enhancement provided by $^4$He/$^3$He occurs for valley-bottom samples, where most of the recent (< 1.5 Ma) exhumation is concentrated. In these settings, the $^4$He/$^3$He data increase the temporal resolution of cooling histories by ~40 % relative to conventional bulk AHe ages. In contrast, the improvement is limited to ~5% for summit areas (Fig. 11c). Relying solely on bulk AHe ages would therefore provide insufficient resolution to detect the Quaternary exhumation of the Rhône Valley, highlighting the critical value of $^4$He/$^3$He thermochronometry for resolving young, low-temperature cooling events.

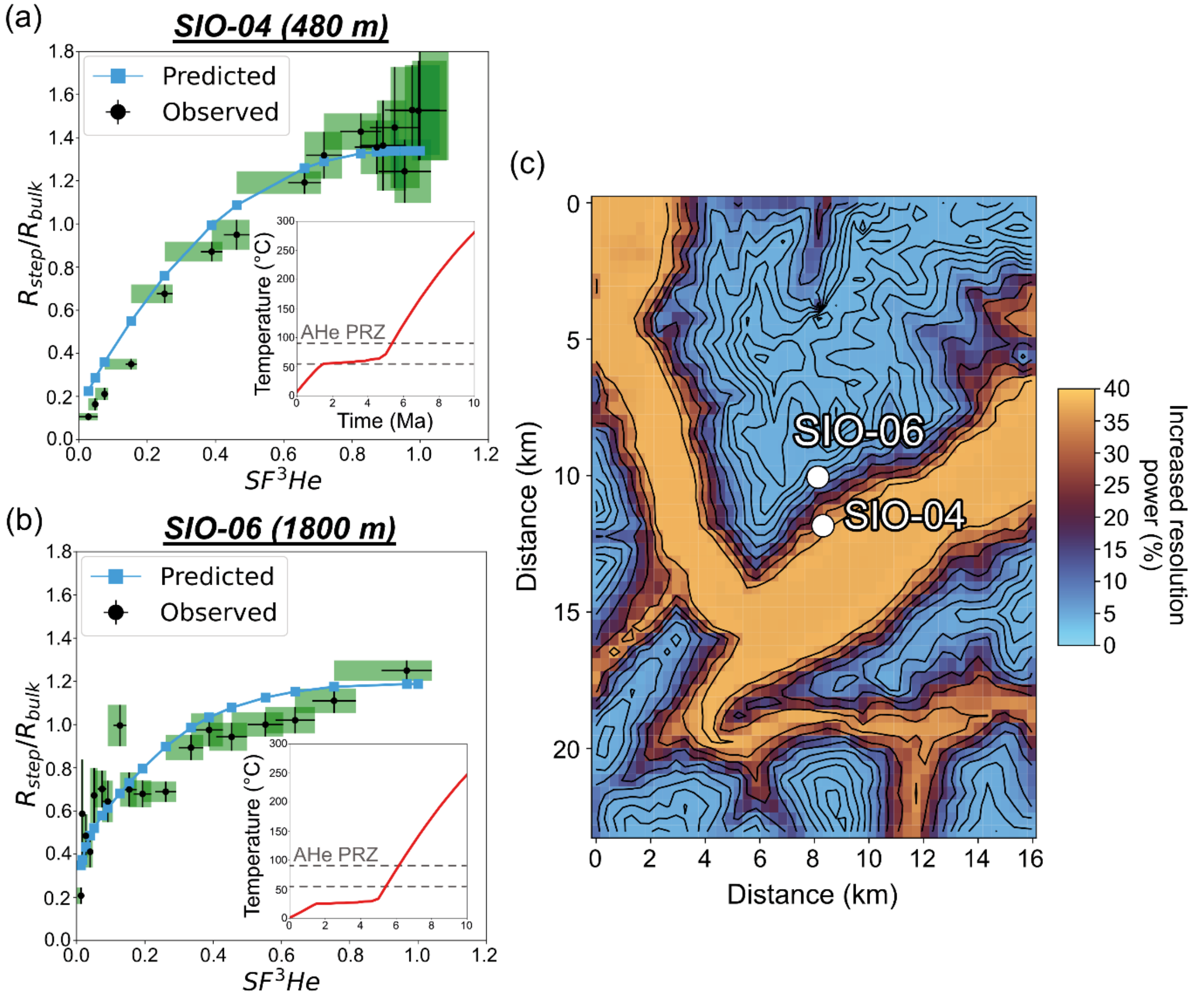

**Figure 11**. Pecube forward modelling of $^4$He/$^3$He data in the Rhône valley (Switzerland). The modelling reproduces the study of Valla et al. (2012), who inferred 1-1.5 km valley incision by glaciation since 1.0±0.5 Ma (see text for more details). Predicted apatite $^4$He/$^3$He spectra are shown together with observed spectra for (a) the valley bottom sample (SIO-04) and

(b) the highest elevation sample (SIO-06) along with their inferred cooling history. The spatial distribution of the increased resolution power (IRP) is shown in (c), with sample locations shown as white circles. The location of the DEM is indicated in Figure 9.

### 4.2 Active development of PecubeGUI

Current development efforts in PecubeGUI aim to broaden the range of supported low-temperature thermochronometers by incorporating trapped-charge dating methods. These techniques have traditionally been applied to constrain sediment burial histories (e.g., Madsen and Murray, 2009) or ages of archaeological features (e.g., Schmidt et al., 2025), and more recently also for surface-exposure dating (e.g., Lehman et al, 2020). Trapped-charge systems rely on the accumulation of electrons in crystal defects (i.e., traps) following their eviction from an atom by environmental radiation. The thermally assisted release of these electrons forms the basis for their use as thermochronometers (see King et al., 2016 for a comprehensive review). Because trapped-charge systems are sensitive to temperatures from ~100°C down to near-surface temperature conditions, they are considered as ultra-low-temperature thermochronometers. Methods in this category include quartz and feldspar thermoluminescence (TL), Optically Stimulated Luminescence (OSL), Infra-red Stimulated Luminescence (IRSL) and quartz Electron Spin Resonance (ESR).

Unlike traditional thermochronometers, trapped-charge systems have finite electron-storage capacity and therefore can reach saturation, imposing an upper age limit beyond which additional signal accumulation cannot be recorded. This characteristic restricts their suitability primarily to rapidly exhuming regions (>1 km.Myr$^{-1}$), although some systems, notably Quartz ESR, possess saturation limits permitting signal accumulation over $10^7$ yr timescales. Despite the constraint imposed by saturation, trapped-charge methods have recently demonstrated their usefulness for reconstructing landscape evolution at Quaternary timescales (Bartz et al., 2024; Herman et al., 2010b; King et al., 2020; Wen et al., 2024). Their ability to capture young, low-temperature cooling signals significantly enhances the temporal resolution of reconstructed thermal histories relative to conventional apatite (U-Th)/He or fission-track systems.

The evolution of trapped-charge signals on laboratory and geological timescales has been investigated through the development of numerical models over the past decade. Implementation in Pecube will focus on trapped-charge models already used in thermochronological applications. These models include the localised-transition model (Jain et al., 2015), the gaussian distributed trap depth model (King et al., 2020; Lambert, 2018), the band-tail states model (Li and Li, 2013), and the general order kinetic model (Guralnik et al., 2015).

## 5. Conclusion

In this contribution, we introduce PecubeGUI, a new open-access graphical user interface designed to modernise and significantly simplify use of the Pecube thermal-kinematic modelling code. Alongside the interface, we present major updates to Pecube itself, including the implementation of modern radiation-damage models for the apatite and zircon (U–Th)/He systems and the integration of ultra-low temperature thermochronometric tools such as apatite $^4$He/$^3$He and trapped-charge methods (ongoing development). We have also incorporated improvements to the implementation of thermal parameters. These additions substantially broaden the range of thermal and exhumation histories that Pecube can reliably resolve, particularly in relatively slowly exhuming settings and on short (Quaternary) timescales, for which previous diffusion models often proved inadequate.

The expanded thermochronometric capabilities allow Pecube to address key challenges in low-temperature thermochronology, such as resolving Quaternary cooling events and detecting subtle differences in how surface processes and tectonic forcing are recorded by thermochronometer data. Our demonstration using $^4$He/$^3$He spectra highlights the increased temporal resolution gained when combining traditional bulk (U–Th)/He measurements with spatial helium-distribution data, illustrating the potential of Pecube to support more nuanced interpretations of recent landscape evolution. Similarly, the current incorporation of trapped-charge systems opens pathways for modelling ultra-low-temperature signals that are especially valuable for constraining late-stage geomorphic processes.

By lowering the technical barrier to model setup, visualisation, and interpretation, PecubeGUI is intended to make thermo-kinematic modelling accessible to a broader range of users, including researchers who may not have prior experience with numerical modelling. The open-access nature of both the interface and the underlying code ensures transparency, reproducibility, and community-driven improvement. We anticipate that these developments will foster wider adoption of Pecube within the thermochronology community and promote new applications across tectonics, geomorphology, and Earth-surface process research.

*Code and data availability.* The source code of the user interface PecubeGUI will be available on github at the time of publication, as well as the source code of Pecube v4.3. For the peer-review process, executables of the PecubeGUI software are provided.

*Author contributions.* MB designed and developed the PecubeGUI package, PvdB, CC and JB provided support for the design and development of the PecubeGUI package, PvdB and GEK provided financial support, XR provided the python package for plotting Pecube model output, WG provided the code for helium diffusion, all other authors contributed to the preparation of the manuscript.

*Competing interests.* One of the (co-)authors (GEK) is a member of the editorial board of *Geochronology*. No other competing interests to be declared.

*Acknowledgements*. We address special thanks to Jean Braun, Lingxiao Gong and Isabel Wapenhans for testing the beta version of the interface and for providing feedback. The work described here was funded by the European Research Council (ERC) under the European Union's Horizon 2020 research and innovation programme (ERC Advanced grant No. 834271 to P.v.d.B and Starting grant No. 851614 to G.E.K.).

## References

Abbey, A. L., Wildman, M., Stevens Goddard, A. L., and Murray, K. E.: Thermal history modeling techniques and interpretation strategies: Applications using QTQt. Geosphere, 19(2), 493-530, https://doi.org/10.1130/GES02528.1, 2023.

Ahrens, J., Geveci, B., and Law, C.: Paraview: An end-user tool for large data visualization. The visualization handbook, 717(8), 2005.

Ault, A. K., Gautheron, C., and King, G. E.: Innovations in (U–Th)/He, fission track, and trapped charge thermochronometry with applications to earthquakes, weathering, surface-mantle connections, and the growth and decay of mountains, Tectonics, 46, 627–35, https://doi.org/10.1029/2018tc005312, 2019.

Bartz, M., King, G. E., Bernard, M., Herman, F., Wen, X., Sueoka, S., Tsukamoto, S., Braun, J., and Tagami, T.: The impact of climate on relief in the northern Japanese Alps within the past 1 Myr–The case of the Tateyama mountains. Earth and Planetary Science Letters, 644, https://doi.org/10.1016/j.epsl.2024.118830, 2024.

Bernard, M.: PecubeGUI documentation. https://pecubegui-doc.readthedocs.io/en/latest/index.html, last access: 11 February 2026.

Bouscary, C., King, G. E., Grujic, D., Lavé, J., Almeida, R., Hetényi, G., and Herman, F.: Sustained deformation across the Sub-Himalayas since 200 ka, Geology, 52, 72–76, https://doi.org/10.1130/g51656.1, 2024.

Braun, J.: Quantifying the effect of recent relief changes on age–elevation relationships. Earth and Planetary Science Letters, 200(3-4), 331-343, https://doi.org/10.1016/S0012-821X(02)00638-6, 2002.

Braun, J.: Pecube: A new finite-element code to solve the 3D heat transport equation including the effects of a time-varying, finite amplitude surface topography. Computers & Geosciences, 29(6), 78s://doi.org/10.1016/S0098-3004(03)00052-9, 2003.

Braun, J., and Robert, X.: Constraints on the rate of post-orogenic erosional decay from low-temperature thermochronological data: Application to the Dabie Shan, China. Earth Surface Processes and Landforms, 30(9), 1203-1225, 2005.

Braun, J., van der Beek, P., Valla, P., Robert, X., Herman, F., Glotzbach, C., Pedersen, V., Perry, C., Simon-Labric, T, and Prigent, C.: Quantifying rates of landscape evolution and tectonic processes by thermochronology and numerical modeling of crustal heat transport using PECUBE. Tectonophysics, 524, https://doi.org/10.1016/j.tecto.2011.12.035, 2012.

Braun, J., Stippich, C., and Glasmacher, U. A.: The effect of variability in rock thermal conductivity on exhumation rate estimates from thermochronological data. Tectonophysics, 690, 288-297, https://doi.org/10.1016/j.tecto.2016.09.027, 2016.

Campani, M., Herman, F., and Mancktelow, N.: Two-and three-dimensional thermal modeling of a low-angle detachment: Exhumation history of the Simplon Fault Zone, central Alps. Journal of Geophysical Research: Solid Earth, 115, https://doi.org/10.1029/2009JB007036, 2010.

Carslaw, H. S., and Jaeger, C. J.: Conduction of Heat in Solids, 3rd ed., Oxford, Clarendon, ISBN 0198533683, 1959.

Dodson, M. H.: Closure temperature in cooling geochronological and petrological systems, Contributions to Mineralogy and Petrology, 40, 259–274, https://doi.org/10.1007/bf00373790, 1973.

Farley, K. A.: Helium diffusion from apatite: General behavior as illustrated by Durango fluorapatite. Journal of Geophysical Research: Solid Earth, 105(B2), 2903, https://doi.org/10.1029/1999JB900348, 2000.

Farley, K. A., Wolf, R. A., and Silver, L. T.: The effects of long alpha-stopping distances on (U-Th)/He ages. Geochimica et Cosmochimica Acta, 60(21), 4223, https://doi.org/10.1016/S0016-7037(96)00193-7, 1996.

Fitzgerald, P. G. and Malusà, M. G.: Concept of the exhumed Partial Annealing (Retention) Zone and age-elevation profiles in thermochronology, in: Fission-Track Thermochronology and its Application to Geology, edited by: Malusà, M. G. and Fitzgerald, P. G., Springer International Publishing, Cham, 165–189, https://doi.org/10.1007/978-3-319-89421-8_9, 2019.

Flowers, R. M., Ketcham, R. A., Shuster, D. L., and Farley, K. A.: Apatite (U–Th)/He thermochronometry using a radiation damage accumulation and annealing model, Geochimica et Cosmochimica Acta, 73, 2347–2365, https://doi.org/10.1016/j.gca.2009.01.015, 2009.

Flowers, R. M., Zeitler, P. K., Danišík, M., Reiners, P. W., Gautheron, C., Ketcham, R. A., Metcalf, J. R., Stockli, D. F., Enkelmann, E., and Brown, R. W.: (U-Th)/He chronology: Part 1. Data, uncertainty, and reporting, Geological Society of America Bulletin, 135, 104–136, https://doi.org/10.1130/b36266.1, 2023a.

Flowers, R. M., Ketcham, R. A., Enkelmann, E., Gautheron, C., Reiners, P. W., Metcalf, J. R., Danišík, M., Stockli, D. F., and Brown, R. W.: (U-Th)/He chronology: Part 2. Considerations for evaluating, integrating, and interpreting conventional individual aliquot data, Geological Society of America Bulletin, 135, 137–161, https://doi.org/10.1130/b36268.1, 2023b.

Gallagher, K.: Transdimensional inverse thermal history modeling for quantitative thermochronology. Journal of Geophysical Research: Solid Earth, 117(B2), https://doi.org/10.1029/2011JB008825, 2012.

Gautheron, C., Djimbi, D. M., Roques, J., Balout, H., Ketcham, R. A., Simoni, E., Pik, R., Seydoux-Guillaume, A.M., Tassan-Got, L., and Tassan-Got, L.: A multi-method, multi-scale theoretical study of He and Ne diffusion in zircon. Geochimica et Cosmochimica Acta, 268, 348-367, 2020.

Gautheron, C., Tassan-Got, L., Barbarand, J., and Pagel, M.: Effect of alpha-damage annealing on apatite (U–Th)/He thermochronology. Chemical Geology, 266(3-4), 157-170, https://doi.org/10.1016/j.chemgeo.2009.06.001, 2009.

Ginster, U., Reiners, P. W., Nasdala, L., and Chanmuang, C.: Annealing kinetics of radiation damage in zircon. Geochimica et Cosmochimica Acta, 249, 225-246, https://doi.org/10.1016/j.gca.2019.01.033, 2019.

Gong, L., Wapenhans, I., and van der Beek, P.: MATPIVoT – MATLAB toolbox for PecubeGUI inversion plotting. Zenodo. https://doi.org/10.5281/zenodo.17110622, 2025.

Guenthner, W. R.: Implementation of an alpha damage annealing model for zircon (U-Th)/He thermochronology with comparison to a zircon fission track annealing model. Geochemistry, Geophysics, Geosystems, 22(2), e2019GC008757, https://doi.org/10.1029/2019GC008757, 2021.

Guenthner, W. R., Reiners, P. W., Ketcham, R. A., Nasdala, L., and Giester, G.: Helium diffusion in natural zircon: Radiation damage, anisotropy, and the interpretation of zircon (U-Th)/He thermochronology. American Journal of Science, 313(3), 145-198, https://doi.org/10.2475/03.2013.01, 2013.

Guralnik, B., Li, B., Jain, M., Chen, R., Paris, R. B., Murray, A. S., Li, S., Pagonis, V., Valla, P.G., and Herman, F.: Radiation-induced growth and isothermal decay of infrared-stimulated luminescence from feldspar. Radiation Measurements, 81, 224-231, 2015.

Harrison, M. T.: Diffusion of $^{40}$Ar in hornblende. Contributions to Mineralogy and Petrology, 78(3), 324-331, https://doi.org/10.1007/BF00398927, 1982.

Herbert, T. D.: The Mid-Pleistocene Climate Transition, Annual Review of Earth and Planetary Sciences, 51, 389–418, https://doi.org/10.1146/annurev-earth-032320-104209, 2023.

Herman, F., Copeland, P., Avouac, J. P., Bollinger, L., Mahéo, G., Le Fort, P., Rai, S., Foster, D., Pêcher, A, Stüwe, K, and Henry, P.: Exhumation, crustal deformation, and thermal structure of the Nepal Himalaya derived from the inversion of thermochronological and thermobarometric data and modeling of the topography. Journal of Geophysical Research: Solid Earth, 115(B6), B06407, https://doi.org/10.1029/2008JB006126, 2010a.

Herman, F., Rhodes, E. J., Braun, J., and Heiniger, L.: Uniform erosion rates and relief amplitude during glacial cycles in the Southern Alps of New Zealand, as revealed from OSL-thermochronology. Earth and Planetary Science Letters, 297(1-2), 183-189, https://doi.org/10.1016/j.epsl.2010.06.019, 2010b.

Jain, M., Sohbati, R., Guralnik, B., Murray, A. S., Kook, M., Lapp, T., Prasad, A.K., Thomsen, K.J., and Buylaert, J. P.: Kinetics of infrared stimulated luminescence from feldspars. *Radiation Measurements*, *81*, 242-250, 2015.

Ketcham, R. A.: Forward and inverse modeling of low-temperature thermochronometry data. Reviews in Mineralogy and Geochemistry, 58, 275, https://doi.org/10.2138/rmg.2005.58.11, 2005.

Ketcham, R. A.: Thermal history inversion from thermochronometric data and complementary information: New methods and recommended practices, Chemical Geology, 653, 122042, https://doi.org/10.1016/j.chemgeo.2024.122042, 2024.

Ketcham, R. A., Carter, A., Donelick, R. A., Barbarand, J., and Hurford, A. J.: Improved modeling of fission-track annealing in apatite. American Mineralogist, 92(5-6), 799-810, https://doi.org/10.2138/am.2007.2281, 2007.

King, G. E., Guralnik, B., Valla, P. G., and Herman, F.: Trapped-charge thermochronometry and thermometry: A status review. Chemical Geology, 446, 3-17, https://doi.org/10.1016/j.chemgeo.2016.08.023, 2016.

King, G. E., Tsukamoto, S., Herman, F., Biswas, R. H., Sueoka, S., and Tagami, T.: Electron spin resonance (ESR) thermochronometry of the Hida range of the Japanese Alps: validation and future potential. Geochronology, 2(1), 1-15, https://doi.org/10.5194/gchron-2-1-2020, 2020.

Lehmann, B., Herman, F., Valla, P. G., King, G. E., Biswas, R. H., Ivy-Ochs, S., Steinemann, O., and Christl, M.: Postglacial erosion of bedrock surfaces and deglaciation timing: New insights from the Mont Blanc massif (western Alps). Geology, 48(2), 139-144, https://doi.org/10.1130/G46585.1, 2020.

Li, B., and Li, S. H.: The effect of band-tail states on the thermal stability of the infrared stimulated luminescence from K-feldspar. Journal of Luminescence, 136, 5-10, 2013.

Lovera, O. M., Richter, F. M., and Harrison, T. M.: Diffusion domains determined by $^{39}$Ar released during step heating. Journal of Geophysical Research: Solid Earth, 96(B2), 2057-2069, https://doi.org/10.1029/90JB02217, 1991.

Łuszczak, K., Persano, C., Braun, J., and Stuart, F. M.: How local crustal thermal properties influence the amount of denudation derived from low-temperature thermochronometry. Geology, 45(9), 779-782, https://doi.org/10.1130/G39036.1, 2017.

McDannell, K. T., Zeitler, P. K., and Idleman, B. D.: Relict topography within the Hangay mountains in central Mongolia: Quantifying long-term exhumation and relief change in an old landscape. Tectonics, 37(8), 2531-2558, https://doi.org/10.1029/2017TC004682, 2018.

Madsen, A. T., and Murray, A. S.: Optically stimulated luminescence dating of young sediments: A review. Geomorphology, 109(1-2), 3-16, 2009.

Murray, K. E., Goddard, A. L. S., Abbey, A. L., and Wildman, M.: Thermal history modeling techniques and interpretation strategies: Applications using HeFTy. Geosphere, 18(5), 1622-1642, https://doi.org/10.1130/GES02500.1, 2022.

NASA Shuttle Radar Topography Mission (SRTM): Shuttle Radar Topography Mission (SRTM) Global. Distributed by OpenTopography, https://doi.org/10.5069/G9445JDF, 2013.

Olivetti, V., Balestrieri, M. L.., Faccenna, C., and Stuart, F. M.: Dating the topography through thermochronology: Application of Pecube code to inverted vertical profile in the eastern Sila Massif, southern Italy. Italian Journal of Geosciences, 136(3), 321-336, https://doi.org/10.3301/IJG.2016.09, 2016.

Piper, M., and Hutton, E.: CSDMS Topography data component (v0.8.5). Zenodo. https://doi.org/10.5281/zenodo.13340258, 2024.

Reiners, P. W., and Brandon, M. T.: Using thermochronology to understand orogenic erosion. Annual Review of Earth and Planetary Sciences, 34(1), 419-466, https://doi.org/10.1146/annurev.earth.34.031405.125202, 2006.

Reiners, P. W., Spell, T. L., Nicolescu, S., and Zanetti, K. A.: Zircon (U-Th)/He thermochronometry: He diffusion and comparisons with $^{40}$Ar/$^{39}$Ar dating. Geochimica et Cosmochimica Acta, 68(8), 1857-1887, https://doi.org/10.1016/j.gca.2003.10.021, 2004.

Robert X.: pyPlotPecube, a Python module to plot PECUBE forward and inverse modeling results. Zenodo. https://doi.org/10.5281/zenodo.5521061, 2021.

Robert, X., van der Beek, P., Braun, J., Perry, C., and Mugnier, J. L.: Control of detachment geometry on lateral variations in exhumation rates in the Himalaya: Insights from low-temperature thermochronology and numerical modelling. Journal of Geophysical Research: Solid Earth, 116(B5), https://doi.org/10.1029/2010JB007893, 2011.

Sambridge, M.: Geophysical inversion with a neighbourhood algorithm—I. Searching a parameter space, Geophysical Journal International, 138, 479–494, https://doi.org/10.1046/j.1365-246x.1999.00876.x, 1999a.

Sambridge, M.: Geophysical inversion with a neighbourhood algorithm—II. Appraising the ensemble. Geophysical Journal International, 138(3), 727-746, https://doi.org/10.1046/j.1365-246x.1999.00900.x, 1999b.

Schildgen, T. F., Balco, G., and Shuster, D. L.: Canyon incision and knickpoint propagation recorded by apatite $^{4}$He/$^{3}$He thermochronometry. Earth and Planetary Science Letters, 293(3-4), 377-387, https://doi.org/10.1016/j.epsl.2010.03.009, 2010.

Schmidt, C., Veres, D., Murătoreanu, G., Cosac, M., Niţă, L., Vasile, Ş., Şerbănescu, G. S., and Bartok, I. E.: Evidence for the oldest Middle Palaeolithic cave occupation in the Romanian Carpathians. Journal of Quaternary Science, 40(1), 22-35, https://doi.org/10.1002/jqs.3667, 2025.

Shuster, D. L., Farley, K. A., Sisterson, J. M., and Burnett, D. S.: Quantifying the diffusion kinetics and spatial distributions of radiogenic $^{4}$He in minerals containing proton-induced $^{3}$He. Earth and Planetary Science Letters, 217(1-2), 19-32, https://doi.org/10.1016/S0012-821X(03)00594-6, 2004.

Shuster, D. L., Cuffey, K. M., Sanders, J. W., and Balco, G.: Thermochronometry reveals headward propagation of erosion in an alpine landscape. Science, 332(6025), 84-88, DOI: 10.1126/science.1198401, 2011.

Shuster, D. L., Flowers, R. M., and Farley, K. A.: The influence of natural radiation damage on helium diffusion kinetics in apatite. Earth and Planetary Science Letters, 249(3-4), 148-161, https://doi.org/10.1016/j.epsl.2006.07.028, 2006.

Stephenson, J., Gallagher, K., and Holmes, C. C.: Low temperature thermochronology and strategies for multiple samples: 2: Partition modelling for 2D/3D distributions with discontinuities. Earth and Planetary Science Letters, 241(3-4), 557-570, 2006.

Sullivan, B., and Kaszynski, A.: PyVista: 3D plotting and mesh analysis through a streamlined interface for the Visualization Toolkit (VTK) (v0.45.0). Zenodo. https://doi.org/10.5281/zenodo.15244303, 2025.

Tremblay, M. M., Fox, M., Schmidt, J. L., Tripathy-Lang, A., Wielicki, M. M., Harrison, T. M., Zeitler, P. K., and Shuster, D. L.: Erosion in southern Tibet shut down at ∼10 Ma due to enhanced rock uplift within the Himalaya. Proceedings of the National Academy of Sciences, 112(39), 12030-12035, https://doi.org/10.1073/pnas.1515652112, 2015.

Valla, P. G., Shuster, D. L., and van der Beek, P. A.: Significant increase in relief of the European Alps during mid-Pleistocene glaciations. Nature Geoscience, 4(10), 688-692, https://doi.org/10.1038/ngeo1242, 2011.

Valla, P. G., van der Beek, P. A., Shuster, D. L., Braun, J., Herman, F., Tassan-Got, L., and Gautheron, C.: Late Neogene exhumation and relief development of the Aar and Aiguilles Rouges massifs (Swiss Alps) from low-temperature thermochronology modeling and $^{4}$He/$^{3}$He thermochronometry. Journal of Geophysical Research: Earth Surface, 117(F1), https://doi.org/10.1029/2011JF002043, 2012.

Vermeesch, P., and Tian, Y.: Thermal history modelling: HeFTy vs. QTQt. Earth-Science Reviews, 139, 279-290, 2014.

Wapenhans, I., Gong, L., and van der Beek, P.: PyPIVoT (PecubeGUI Visualization Tools). Zenodo. https://doi.org/10.5281/ZENODO.17079595, 2025.

Wen, X., Bartz, M., Schmidt, C., and King, G. E.: ESR and luminescence thermochronometry of the Rhône valley, Switzerland. Quaternary Geochronology, 80, 101496, https://doi.org/10.1016/j.quageo.2023.101496, 2024.

Whipp Jr, D. M., and Ehlers, T. A.: Influence of groundwater flow on thermochronometer-derived exhumation rates in the central Nepalese Himalaya. Geology, 35(9), 851-854, https://doi.org/10.1130/G23788A.1, 2007.

Willett, C. D., Fox, M., and Shuster, D. L.: A helium-based model for the effects of radiation damage annealing on helium diffusion kinetics in apatite. Earth and Planetary Science Letters, 477, 195-204, https://doi.org/10.1016/j.epsl.2017.07.047, 2017.

Wolff, R., Hetzel, R., Dunkl, I., and Anczkiewicz, A. A.: New constraints on the exhumation history of the western Tauern Window (European Alps) from thermochronology, thermokinematic modeling, and topographic analysis. International Journal of Earth Sciences, 110(8), 2955-2977, https://doi.org/10.1007/s00531-021-02094-w, 2021.